



Dual charge-accepting engineering modified AgIn₅S₈/CdS quantum dots for efficient photocatalytic hydrogen evolution overall H₂S splitting

Anqiang Jiang ^{a,b}, Heng Guo ^{a,b,*}, Shan Yu ^{a,b,*}, Fengying Zhang ^{a,b}, Tingyu Shuai ^c, Yubin Ke ^d, Peng Yang ^{a,b}, Ying Zhou ^{a,b,*}

^a State Key Laboratory of Oil and Gas Reservoir Geology and Exploitation, Southwest Petroleum University, Chengdu 610500, China

^b School of New Energy and Materials, Southwest Petroleum University, Chengdu 610500, China

^c College of Materials Science and Engineering, Sichuan University, Chengdu 610065, China

^d Spallation Neutron Source Science Center, Institute of High Energy Physics, Chinese Academy of Sciences, Dongguan 523808, China



ARTICLE INFO

Keywords:

AgIn₅S₈/CdS core/shell quantum dots
Inorganic ligand
Transient absorption spectroscopy
Hydrogen sulfide degradation
Hydrogen production

ABSTRACT

Low charge carrier separation and transfer efficiency continues to be the major obstacle to harvest solar energy to split hydrogen sulfide (H₂S) as hydrogen source for H₂ production with value-added utilization for waste by-products. Herein, we designed a Type-II core/shell AgIn₅S₈/CdS (AIS/CdS) quantum dots (QDs) photocatalyst capped with short-chain inorganic sulfide ion (S²⁻) ligand with dual charge-accepting engineering to promote charge carrier extraction and faster photogenerated electron transfer. Transient absorption spectroscopy analysis demonstrates that the excited electrons are fast injected into CdS shell from AIS core within 1.7 ps, instead of transferring to sub-bandgap states. Consequently, the highest photocatalytic hydrogen evolution rate of AIS/CdS QDs with S²⁻ ligand is 12.74 mmol g⁻¹ h⁻¹ that is more than four times of pristine AIS core. This work offers insightful guidance on the rational design of charge-accepting engineering QDs-based photocatalysts, thereby stimulating solar to hydrogen generation and resource utilization of pollutants.

1. Introduction

Photocatalytic overall water splitting for the green generation of hydrogen (H₂) presents a promising and sustainable paradigm for cutting-edge solar energy utilization technology due to its potential applications in supplying clean and renewable energy [1–5]. Nevertheless, the oxidative half-reaction in photocatalytic water splitting, facing the fundamental issues of slow kinetics and low energy conversion efficiency, is the principal bottleneck of photocatalytic overall water splitting [6–9]. In particular, the energy difference between the oxidation potential of water and the top of the valence band of the photocatalyst is commonly insufficient to drive the multielectron transfer and proton-coupled reaction involved in water oxidation [10, 11]. Consequently, numerous reports solely concentrate on either hydrogen or oxygen evolution half-reaction with the addition of sacrificial agent, which facilitate a charge transfer process but result in complex products and reduce photocatalysis economy [12–15].

Hydrogen sulfide (H₂S), as an abundant but highly toxic and corrosive gas generated with the exploiting of acid gas reservoirs, is extremely

hazardous, and in certain situations it can even be fatal both for animals and human beings [16]. Alternatively, it is also considered to be a potential source of H₂ because the splitting energy of H₂S (0.14 V or 33 kJ mol⁻¹) is much more readily than that of H₂O (1.23 V, 273 kJ mol⁻¹) [17,18]. The addition of H₂S in the photocatalytic water splitting reaction medium can not only avoid the issue of sluggish water oxidation kinetics and promote the evolution of H₂, but also realize the environmentally friendly treatment of H₂S [19,20]. However, the design and development of high-efficient photocatalysts, as well as resistance to hydrogen sulfide toxicity, continue to be limitations of the photocatalytic H₂ generation and co-processing H₂S system.

Metal chalcogenides, a good photocatalytic and photoelectrochemical material, exhibit more negative conduction band locations and narrower band gaps, as well as stronger poison resistance, and is regarded as ideal photocatalyst for overall H₂S splitting [19,21]. Recently, ternary I-III-VI quantum dots (QDs), like AgIn₅S₈ (AIS)-based QDs with low toxic elements, broad light absorption range, and high carrier mobility via composition control, have attracted wide attention for solar-driven hydrogen generation or photocatalytic degradation

* Corresponding authors at: State Key Laboratory of Oil and Gas Reservoir Geology and Exploitation, Southwest Petroleum University, Chengdu 610500, China
E-mail addresses: heng.guo@swpu.edu.cn (H. Guo), yushan@mail. ipc.ac.cn (S. Yu), yzhou@swpu.edu.cn (Y. Zhou).

[22–26]. However, the unsaturated surface atom bonding causes QDs surface defects that give rise to non-radiative recombination centers, hindering photogenerated carriers for participation in subsequent reactions [5,27,28]. Accordingly, ternary chalcogenide QDs generally exhibit poor long-term stability and low photocatalytic H₂ evolution performance. A major strategy utilized to passivate surface defects was the design and construction of unique core/shell structures [29]. Different charge carrier localization regimes following photoexcitation are related to the energy band arrangements between the core and shell materials, which makes it possible to design the energy band arrangement of the core and shell materials that allows to extract photo-generated electrons or holes to reduce carrier recombination [27,30,31]. Additionally, QD synthesized using conventional colloid technique has a layer of ligand with a lengthy hydrocarbon tail that introduces insulating layers around each QD and significantly lowers the dispersion of QD in aqueous media [32]. Therefore, short chain inorganic ligands, applied after shell or additional defect passivation strategies, provide colloidal stability without hindering charge transfer between particles [32,33].

Herein, we propose a dual charge-accepting-structure strategy for band structure engineering and sulfur-ligand passivation of core-shell AgIn₅S₈/CdS (AIS/CdS) QDs to achieve high-efficient H₂ evolution via H₂S photocatalytic splitting. The type-II alignment structure not only suppresses photogenerated charges recombination due to surface defects, but also promotes the spatial separation of photoexcitation electron-hole pairs. Coupled with the effect of S²⁻ ligand to accelerate hole transfer, the photocatalytic ability of type-II AIS/CdS core-shell QDs is significantly increased (4.16 times) compared to pristine QDs. Wave function calculations demonstrate that type-II AIS/CdS QDs have superior charge transport channels to type-I core-shell QDs. More importantly, time-resolved photoluminescence spectra and transient absorption spectra reveal that AIS/CdS-S QDs show efficient charge carriers extraction from the AIS core and the fast band edge electron transfer (1.7 ps) to realize the performance enhancement. The dual charge accepting-engineering strategy offers a rational and powerful way to extract photogenerated charges from QDs and provides a potential route for developing efficient photocatalytic reactions coupled with resource utilization of pollutants.

2. Experimental

2.1. Synthesis of AIS QDs

The modified hot injection method was used to synthesize AgIn₅S₈ quantum dots (AIS QDs). Typically, silver nitrate (0.1 mmol, AgNO₃, 99.8%, KESHI), indium acetate (0.5 mmol, In(Ac)₃, 99.99%, Aladdin), and 1-octadecene (8.0 mL, ODE, 90%, Aladdin) are mixed in a flask, degassed with N₂ for 30 min at room temperature, then heated to 90 °C. Then, 1-dodecanethiol (1 mL, DDT, 98%, Aladdin) was injected into the reaction flask. To produce QDs of various sizes, the reaction solution was heated to various temperatures (130 °C, 140 °C, 150 °C, and 160 °C, respectively). The mixture of sulfur powder (0.8 mmol, S, 99.999%, Adamas-beta) and oleylamine (1.3 mL, OLA, 80%–90%, Aladdin) was quickly injected into the solution while it was being vigorously stirred. Following eight minutes of reaction at the temperature before injection, the solution was cooled with cold water. The unreacted precursors were separated by centrifugation after the solution cooled to room temperature and the products were precipitated with ethanol. The produced AIS QDs were redispersed in normal hexane (n-HEX, AR, Meryer).

2.2. CdS (or ZnS) shell growth

In order to synthesize AIS/CdS QDs, the mixture of S (0.1 mmol) and Cadmium acetate dihydrate (0.1 mmol, Cd(Ac)₂·2 H₂O, 99%, Aladdin) dissolved in the mixed solution of OLA and ODE (the ratio of OLA/ODE is 3/2, in total 5 mL) was injected into the reaction solution mentioned

above, which contained AIS QDs. Then, to regulate shell thickness, the growth of the CdS shell was carried out for periods of 15, 30, 60, and 120 min at the same temperature. The reaction mixture was then chilled with cold water until it reached room temperature. Ethanol was used to precipitate the products, after which the suspension was centrifuged and the supernatant was removed. The n-HEX was used to disperse the AIS/CdS QDs. In order to harvest AIS/ZnS, 0.1 mmol Cd(Ac)₂ was replaced by 0.1 mmol Zinc acetate dihydrate (Zn(Ac)₂·2 H₂O, 99.99%, Aladdin) with the same synthesis method.

2.3. S²⁻ ligand exchange

AIS-S²⁻, AIS/ZnS-S²⁻ and AIS/CdS-S²⁻ QDs were prepared by modifying a known procedure [34]. The ligand exchange process was performed in air. In a typical process, QDs solution (1 mL) containing ~3 mg QDs was mixed with Sodium sulfide hydrate (0.012 g, Na₂S·9 H₂O, 98%, KESHI) dissolved in N-Methylformamide (1 mL, NMF, 99%, Aladdin). The mixture was thoroughly phase-transferred from the n-HEX phase to the NMF phase via being stirred at room temperature for about 10 min. The phase transfer process is easily visible due to the n-HEX (red to colorless) and NMF (colorless to red) phase color changes. The NMF phase was then twice washed in n-HEX to remove any remaining nonpolar organic species. The n-HEX phase was then removed. Following the addition of 3 mL of acetone (99.5%, KESHI), the mixture was centrifuged to remove the supernatant. The precipitate was purified using 0.5 mL formamide (FA, 99%, Aladdin) and 1 mL acetone. The precipitate was dissolved with 1 mL of ultrapure water.

2.4. Characterization methods

X-ray diffraction (XRD) of QDs was carried out with a PANalytical X'pert diffractometer using Cu K_α radiation at 40 kV and 40 mA. A dual anode X-Ray source and an ESCALAB 250Xi electron spectrometer were used to conduct X-ray photoelectron spectroscopy (XPS) on the samples. The C1s peak, at 284.8 eV, served as the standard for all binding energies. Tecnai G2 F20 S-TWIN, FEI TEM was used to measure the TEM images and SAED patterns of QDs. At the China Spallation Neutron Source, small-angle neutron scattering (SANS) experiments were conducted using the general time-of-flight small angle diffractometer. Shimadzu UV-2600 spectrophotometer was used to record UV-vis absorption spectra. A fluorescence spectrophotometer (Hitachi F-7000) was used to measure steady-state photoluminescence spectra (PL). Time-resolved photoluminescence spectra (TRPL) and transient absorption spectra were recorded by Edinburgh FLS1000 fluorescence spectrophotometer and the Harpia-TA spectroscopy system (Harpia, Light conversion), respectively. The light resource of Harpia-TA spectroscopy system was supplied by a femtosecond laser (Pharos, Light conversion) centered at ~1028 nm with pulse repetition rate of 100 kHz and pulse width of ~190 fs. All the spectral measurements were performed at room temperature.

2.5. Photocatalytic H₂ evolution tests

The photocatalytic hydrogen production of as-prepared QDs was conducted in a 100 mL photoreactor. Under strict sealing conditions, hydrogen sulfide (hydrogen sulfide in 2% argon) was pump into the photoreactor containing 50 mL of 0.6 mol L⁻¹ sodium sulfite solution, and the gas pump rate was 30 mL min⁻¹ for an hour. Additionally, in order to balance pressure and poison gas treatment, the reactor must be followed by a tail gas absorption device. A 300-W Xe lamp with a cutoff filter ($\lambda > 420$ nm) was used to illuminate the reactor after injecting 1 mL of the as-prepared aqueous QD solution and 1 mL of CH₄ to serve as an internal standard. The light intensity was then kept at 600 mW cm⁻². Gas chromatography (TM GC-2010 Plus, China, Ar carrier gas, molecular sieve 5 Å, TCD detector) was used to detect the produced H₂ gas.

The apparent quantum yield (AQY) for H₂ evolution was acquired by

a 300-W Xe lamp with a band-pass filter of 365, 500, 550, 600 and 700 nm. The intensities were 0.15, 0.14, 0.14, 0.14 and 0.11 W cm⁻², respectively. The monochromatic light's irradiation area was 2.6 cm⁻². The AQY value was estimated using the following Eq. (1) based on the amount of hydrogen was generated by the photocatalytic process in 1 h.

$$\begin{aligned} AQY\% &= \frac{2 \times \text{number of } H_2}{\text{Number of incident photons}} \times 100\% \\ &= \frac{2 \times R_{H_2} \times N_A \times h \times c}{S \times P \times t \times \lambda} \times 100\% \end{aligned} \quad (1)$$

In this equation, R_{H_2} stands for the amount of evolved hydrogen (in mol), N_A is the Avogadro constant, S is the illumination area, and P and λ are the monochromatic light intensity (W cm⁻²) and wavelength (nm), respectively. t stands for the irradiation time, h for the Planck constant, and c for the speed of light.

2.6. Photoelectrochemical test

On fluorine-tin oxide (FTO) glass that had been cleaned using a sonicator with deionized water, ethanol, and acetone for 15 min, the working electrode was prepared and dried at 60 °C. Tetrabutyl titanate, 3 mL pure ethanol, and 25 μL concentrated hydrochloric acid were mixed to form the TiO₂ solution. The solution was then spin-coated onto the FTO/glass substrates at 4000 rpm for 30 s, followed by 30 min of sintering at 450 °C in an oven. TiO₂ paste (a mixture of TiO₂ nanoparticles with a diameter of 20 ~ 450 nm, 18 NR-AO, Dyesol) was used to tape-cast the mesoporous TiO₂ layer (m-TiO₂ film) on c-TiO₂/FTO substrates from a prior approach. The TiO₂ paste layer was coated, let them dry for 12 min in the air, and then dried for 6 min at 120 °C. The m-TiO₂/c-TiO₂ films were ultimately produced after being annealed at 450 °C for 30 min in air. Vertically submerging in QD solution, two m-TiO₂/c-TiO₂/FTO/glass substrates were spaced at a 1 cm interval apart. For 100 min, a 200 V direct current bias was applied to fabricate QDs-based photoanode. In a three-electrode cell, photocurrent density curves and EIS were obtained using a Hg/HgO (3 M KCl) electrode as the reference electrode and a Pt plate as the counter electrode.

2.7. Theoretical calculation of wave functions

The recombination of 1 S electrons and holes in the QDs is considered to be the cause of the PL emission process. [35] The stationary Schrödinger equation in spherical geometry was solved in COMSOL to calculate the wave functions (a commercial software for finite element simulation). The equation can be written as: [35].

$$\nabla \left(\frac{\hbar^2}{2m^*(r)} \nabla \psi \right) + V(r)\psi = E\psi \quad (2)$$

where the wave functions are normalized using $\int |\psi_{\text{electron or hole}}|^2 dV = 1$, and suitable boundary conditions are applied at the interface. The effective masses of electrons (m_e^*) and holes (m_h^*) were calculated using the bulk values; for example, $m_e^* = 0.21 m_0$ and $m_h^* = 2.72 m_0$ for AIS, $m_e^* = 0.14 m_0$ and $m_h^* = -0.51 m_0$ for CdS, and $m_e^* = 0.24 m_0$ and $m_h^* = -0.86 m_0$ for ZnS. The potentials for electrons and holes in the bulk materials were roughly calculated using the lowest unoccupied molecular orbital level and the highest occupied molecular orbital level, respectively. These levels are 3.80 eV and 6.10 eV for AIS, 3.63 eV and 5.83 eV for CdS, and 3.50 eV and 7.10 eV for ZnS, respectively. In the calculations, the interaction between electrons and holes was disregarded.

2.8. Photoluminescence lifetime fitting

The triple exponential model was used to fit experimental data with Eq. (3): [36].

$$I(t) = \sum A_i e^{-t/\tau_i} \quad (i = 1, 2, 3) \quad (3)$$

where τ is the decay time and A is the relative amplitude of each decay component. The three components result from three distinct radiative recombination processes. The first decay time, τ_1 , corresponds to quick photocarrier recombination on QD surface defects primarily caused by dangling bonds. The second decay time, τ_2 , refers to recombination on QD surface states. The final decay time, τ_3 , corresponds to recombination from the core states. [37–39] The PL decay time (τ_{av}) was calculated by Eq. (4):

$$\tau_{av} = \frac{\sum A_i \tau_i^2}{\sum A_i \tau_i} \quad (i = 1, 2, 3) \quad (4)$$

3. Results and discussion

3.1. Synthesis and characterization

Fig. 1a shows the schematic diagram of the optimization process of QDs, including the synthesis of core AgIn₅S₈ (AIS) QDs, inorganic ZnS or CdS shell coating and surface ligand modification. Here, a modified one-pot two-step thermal injection approach was used to synthesize QDs [24]. On the surface of QDs, the short inorganic S²⁻ ligands (QDs-S) were employed to substitute the long-chain organic ligands (QDs-OLA) [32, 34]. The as-prepared QDs were obtained with different reaction temperature and time. The normalized ultraviolet-visible (UV-vis) absorption and photoluminescence (PL) spectra of QDs dispersed in n-hexane were investigated at room temperature (Fig. S1–S3). Although all absorption spectra do not exhibit a recognizable first excitonic peak, ascribed to delocalization of electrons over manifold electronic states [37, 39, 40], quantum dots synthesized at 140 °C present more obvious absorption band around ~500 nm. PL emission of AIS QD exhibits a wide bandwidth that is attributable to carrier recombination between the donor and acceptor states, instead of band-edge emission [41]. With the reaction temperature increases, the absorption and emission shifts to lower energy (Fig. S1), the latter being more pronounced, indicating growing the particle size and attenuated confinement effect [42]. After ZnS shell passivation, the absorption spectra of core/shell QDs shift to higher energy (Fig. S2). The PL spectra of core/shell QDs further demonstrate the blue-shift, indicating that the shell extends the forbidden band width of AIS and the defect level is more distant in energy leading to a blue-shifted emission [43]. The absorption spectra of AIS/CdS QDs shift to lower energy and exhibit enhanced light absorption with respect to pristine AIS QDs (Fig. S3), which can be attributed to the narrower gap of CdS shell material compared with AIS core. The PL emission peak of AIS/CdS QDs slightly move to higher energy, which is ascribed to the more distant defect level in energy [44]. As we can see in Figs. S2–3, temporal evolution of PL peak was not apparent when shell growth time was more than 60 min. Consequently, we chose the QDs synthesized at 140 °C with a shell growth time of 60 min as the model catalyst for further research.

According to the X-ray diffraction (XRD) pattern in Fig. 1b, all samples exhibited three characteristic diffraction peaks, which could be attributed to the AIS QDs of single-crystal cubic phase (PDF#25–1329), and the strongest diffraction peak matched to the (311) plane, indicating the crystal structure was not changed by shell growth. However, it is difficult to identify cubic AIS QDs from tetragonal AgInS₂ (t-AgInS₂) crystal phase structure by XRD pattern due to the broadened diffraction peaks, but there is proof that AIS QDs were obtained at the given synthesis temperature of 140 °C [45]. Meanwhile, after growing CdS (or ZnS), the intensity of the diffraction peak of AIS/CdS (or AIS/ZnS) core/shell QDs at 47.0°, which corresponds to the peak of cubic phase CdS (PDF#21–0829) or cubic phase ZnS (PDF#05–0566), increases dramatically, indicating the growth of shell.

AIS/CdS QDs exhibit approximately uniform morphology with an

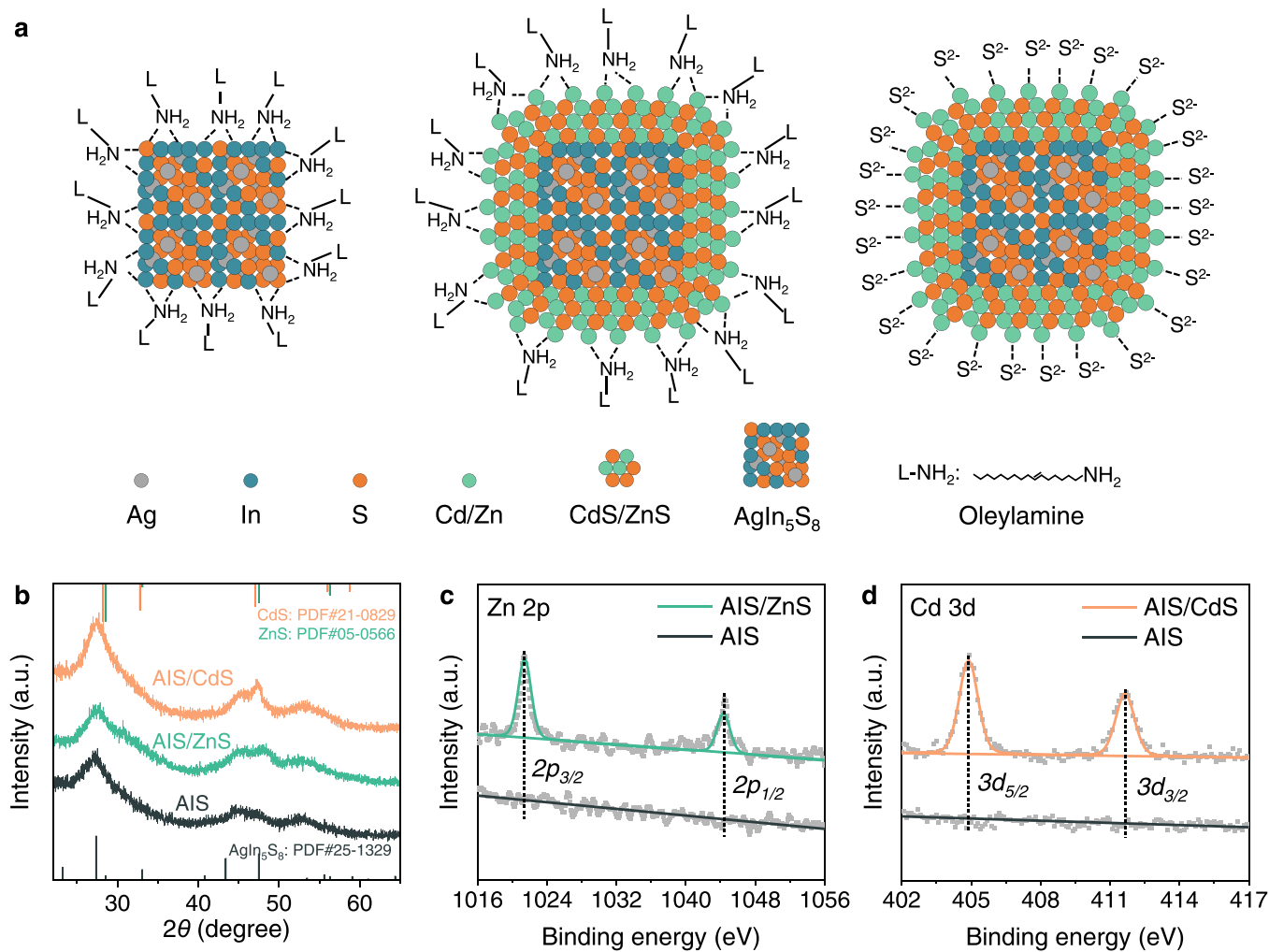


Fig. 1. Modification of QDs from shell growth and surface ligands. a) Illustrative schematic of AIS-OLA QDs, AIS/shell-OLA QDs and AIS/shell-S QDs (The shell is ZnS or CdS). b) XRD patterns of QDs. c) Zn 2p and d) Cd 3d core level spectra in XPS.

average particle size of ≈ 2.8 nm as observed in the transmission electron microscopy (TEM) and size distribution histogram (Fig. S4a and b). High-resolution TEM (HR-TEM) of an individual AIS/CdS QDs displays an interplanar distance of 0.32 nm that matches with characteristic (311) plane (inset in Fig. S4c). However, the absence of a distinct interface between the core QDs (AIS) and the shell material (CdS) was not observed, suggesting epitaxial growth of the CdS shell. Furthermore, the corresponding selected area electron diffraction pattern shows two distinct diffraction rings indexed to (311) and (440) crystal plane of AIS QDs, respectively (Fig. S4d). The surface chemical compositions of AIS, AIS/ZnS and AIS/CdS QDs were obtained by XPS characterization, and the survey spectra are shown in Fig. S5a. The typical chemical states for Ag 3d, In 3d, and S 2p core level spectra are easily distinguishable for all QDs (Fig. S5b-c). The XPS spectrum of core/shell QDs exhibits two additional Cd 3d or Zn 2p peaks. The binding energies of Cd 3d_{5/2} and Cd 3d_{3/2} locating at 404.9 eV and 411.7 eV in Fig. 1c can well match the 3d signal of Cd²⁺ in CdS. A similar result is observed, in which the AIS/ZnS Zn 2p spectrum contains the signal that matches the Zn²⁺ in ZnS (Fig. 1d). These results demonstrate effective ZnS or CdS shell growth and are consistent with the XRD results.

Surface ligands exchange process was carried out under atmospheric environment. The effective phase transition of the treated QDs from hexane (HEX) to N-Methylformamide (NMF), as shown in Fig. 2a, demonstrates the effectiveness of ligand exchange. These S²⁻ capped QDs could be uniformly distributed in water by multiple precipitation and

dissolution. Small-angle neutron scattering (SANS) experiments were carried out for size information based on aqueous solution containing QDs-S. SANS is a technique for studying the mesoscale structure (1–100 nm) inside a material by using elastically scattered neutrons in a restricted angular range [46]. According to Fig. 2b, it can be observed that the scattering intensity of all samples decreases exponentially with the increase of Q value. The scattering intensity of AIS/CdS is obviously lower than others in low Q region, which is probably due to the strong absorption of neutrons by the Cd element. Furthermore, the pair distance distribution function versus size distribution of QDs demonstrates that the levels of aggregation in all quantum dot samples are different (Fig. S6). Following the shell growth, the dispersion of quantum dot samples significantly increased. The least degree of aggregation was found in AIS/CdS QDs, which is more favorable for photocatalytic reaction. UV-vis absorption spectra and PL spectra of QDs before and after ligand exchange are shown in Fig. 2c. Following ligand exchange, the light absorption range of quantum dots narrows slightly, which can be attributed to partial decomposition of quantum dots and the size of quantum dots decreased. Nevertheless, the PL intensity of all QDs following ligand exchange significantly decreased (Fig. 2c), which is attributed to an increase in surface traps and nonradiative relaxation processes [47]. Additionally, the nearly complete removal of the ligand C-H stretching FT-IR bands at 2855 and 2924 cm⁻¹ is indication of effective ligand exchange (Fig. 2d). As a result, we obtained a quantum dot photocatalyst with shell growth and surface ligand modification.

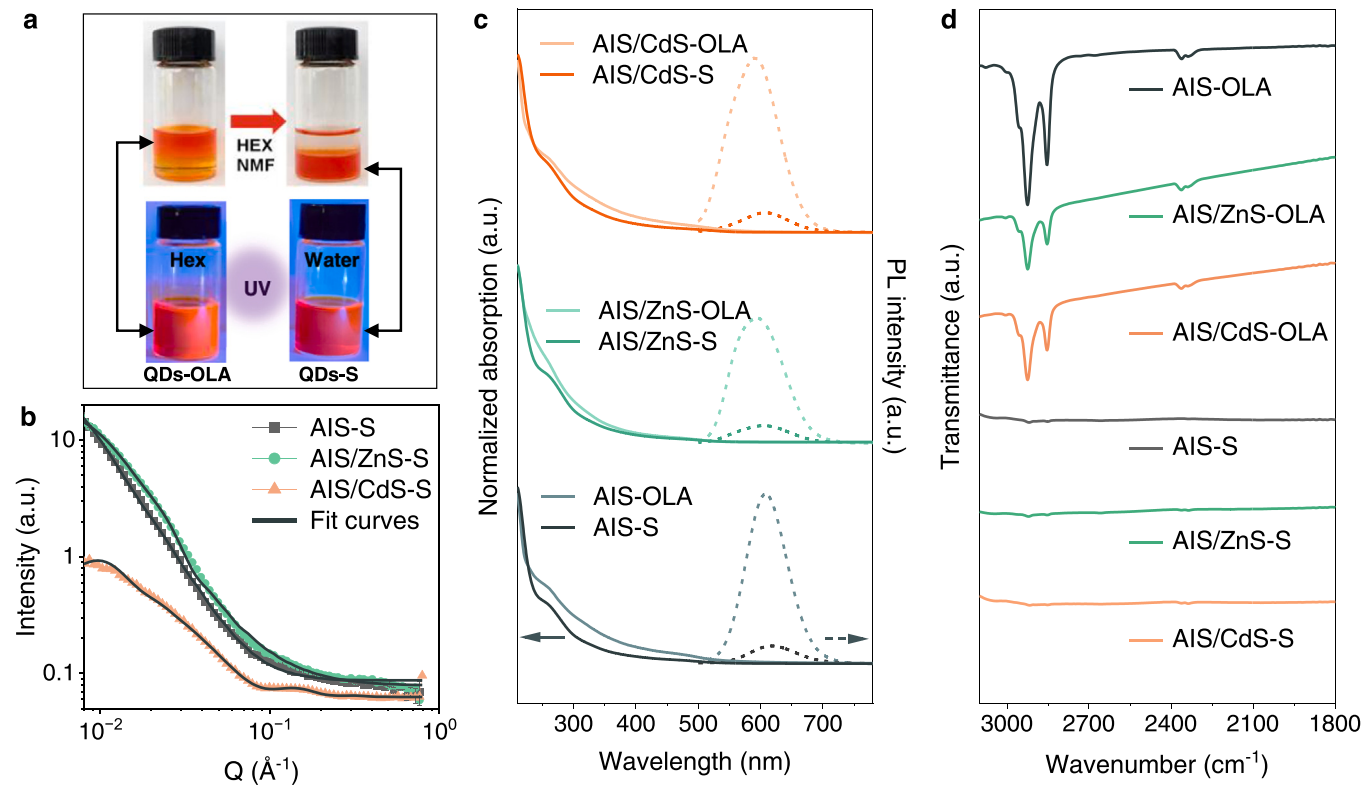


Fig. 2. Transition from QDs-OLA to QDs-S. a) Red-colored QDs undergo the phase transfer from hexane (HEX) to N-Methylformamide (NMF) upon substitution of S^{2-} for the initial organic surface ligands. b) Small-angle neutron scattering data of AIS-S, AIS/ZnS-S, AIS/CdS-S. c) UV-Vis absorption spectra and PL spectra and d) FT-IR spectra of AIS, AIS/ZnS, AIS/CdS QDs before and after ligand exchange.

3.2. Photocatalytic performance

The ligand-exchanged core/shell QDs were subsequently used to carry out the photocatalytic hydrogen evolution via H_2S photodegradation. The effectiveness of photocatalytic decomposition of H_2S for hydrogen production was investigated on AIS-S QDs, AIS/ZnS-S QDs, and AIS/CdS-S QDs in the presence of sulfite as the reaction media (Fig. 3a). The hydrogen production rate of AIS/ZnS and AIS/CdS is 1.23 and 4.16 times than that of AIS ($3.06 \text{ mmol g}^{-1} \text{ h}^{-1}$), respectively. Among them, the decomposition efficiency of AIS/CdS ($12.74 \text{ mmol g}^{-1} \text{ h}^{-1}$) is 3.38 times higher than that of AIS/ZnS ($3.76 \text{ mmol g}^{-1} \text{ h}^{-1}$). The test results demonstrate that the growth of ZnS or CdS shell can efficiently passivate surface defects and boost pristine AIS core photocatalytic degradation of H_2S for hydrogen production. The apparent quantum efficiencies (AQEs) for photocatalytic hydrogen evolution of three samples were then examined with monochromatic light under the same reaction conditions in order to uncover the cause of the increase in photocatalytic activity (Fig. 3b). The AQEs of AIS/CdS increased rapidly in the broad region of 380–600 nm, which reaches to the highest one of 2.71% at 380 nm. Compared to AQEs of AIS and AIS/ZnS, AIS/CdS exhibits noticeably better conversion of incident photons into hydrogen due to its larger light harvesting region and efficient charge transfer process. What's more, transient photocurrent measurements show that AIS QDs responds minimally to light (Fig. 3c). A quick relative light response was observed for both AIS/ZnS and AIS/CdS QDs. Particularly, AIS/CdS QDs showed a greater current density compared with AIS/ZnS QDs, indicating that AIS/CdS QDs interact well with the reaction system. In addition, electrochemical impedance spectroscopy (EIS) data indicate that AIS/CdS QDs exhibit the lowest resistance under simulated sunlight illumination (Fig. 3d). According to the fitting results, the R_{ct} of AIS, AIS/ZnS, and AIS/CdS QDs is 1.3×10^4 , 5.5×10^3 , and $1.5 \times 10^3 \Omega$, respectively; among them, the R_{ct} of AIS/CdS QDs is the smallest, demonstrating enhanced interfacial charge transfer properties. These

findings suggest that a CdS epitaxial growth approach based on AIS core can enhance the effectiveness of solar energy harvesting and more effectively induce photogenerated charge transfer.

3.3. Mechanism investigation

To discover the mechanism of the elevated photocatalytic activity, it is carried out that the band structure of QDs was estimated. Based on the relative alignment of conduction band (CB) and valence band (VB) edges of the materials that are alloyed at the heterointerface, core/shell QDs are typically classified as type I, type II and quasi-type II, which exhibit diverse spatially separated behaviors of positive and negative charges [29,48–50]. The Tauc plots of the AIS quantum dot samples (Fig. S7) show an approximate band gap (E_g), estimated E_g of 2.43 eV. XPS valence band spectrum was further employed to estimate the band positions of AIS QDs (Fig. S8). As shown in Fig. 4a, AIS/ZnS is type-I band structure forasmuch as the CB and VB edge of the synthesized AIS QDs are both situated inside the energy gap of ZnS. The photogenerated electron-hole pairs in this case have a tendency to localize in the AIS core, which offers the lowest energy states for electrons and holes while still restricting the extraction of photoinduced charge in QDs for furthermore energy conversion. In contrast, the lowest energy states of electrons and holes in AIS/CdS QDs, with type-II band structure, lie in the VB of AIS and the CB of CdS, respectively, allowing for the spatial separation of positive and negative charges. It is demonstrated that the photocatalytic hydrogen generation with H_2S degradation reaction could be more effectively promoted by core-shell QDs with the type-II band structure (AIS/CdS). On the one hand, the carrier recombination center is diminished by the ZnS or CdS shell passivation strategy, increasing the photocatalytic activity of the core/shell QDs relative to the pristine AIS QDs. On the other hand, the AIS/CdS QDs with type-II band structure are favorable for spatial charge separation, strengthen the transfer of photogenerated electrons and holes to the reactants [51],

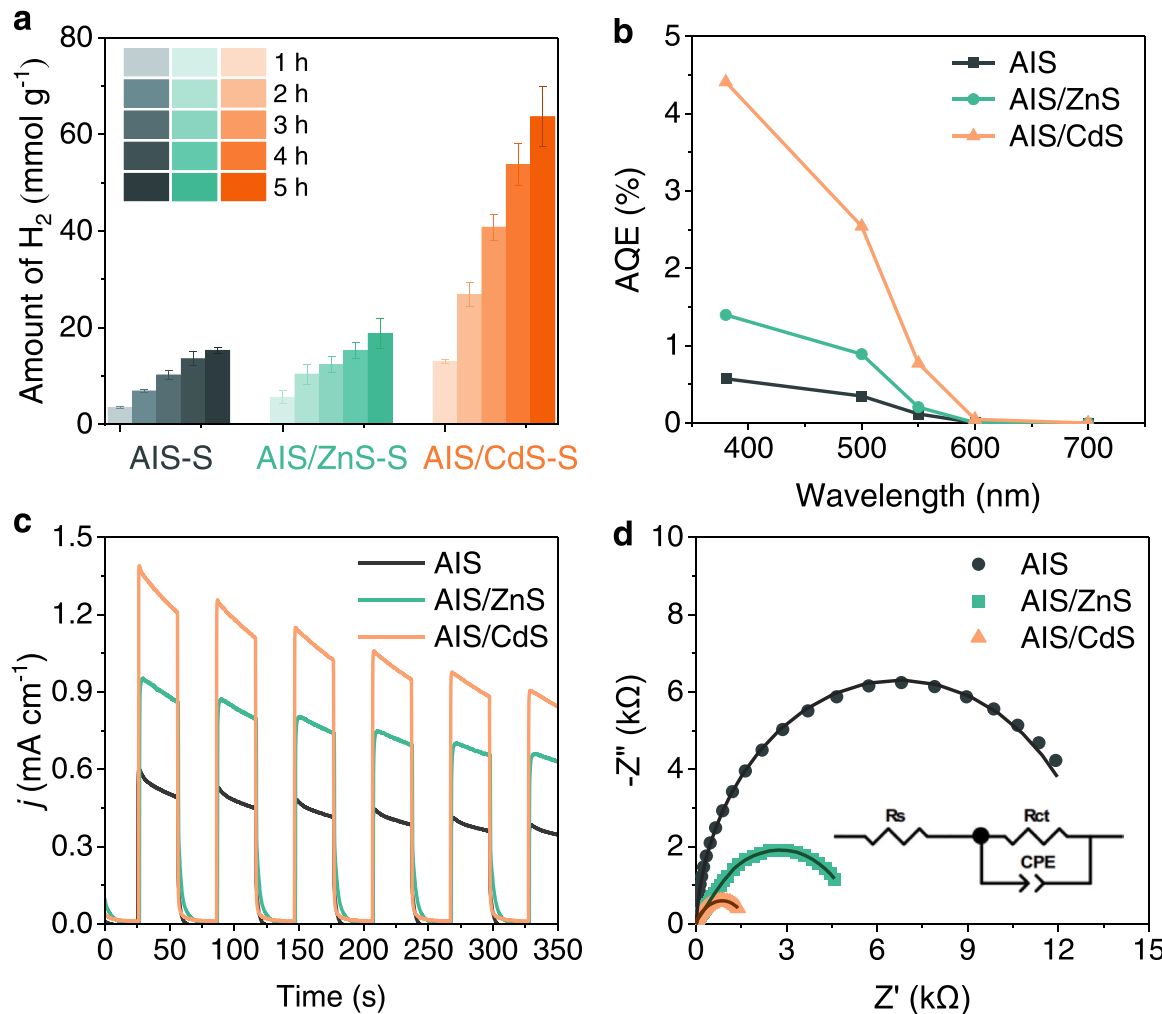


Fig. 3. Photocatalytic H_2 production coupled H_2S degradation. a) H_2 production rates and b) AQE for three QDs. c) Transient photocurrent and d) EIS of AIS, AIS/ZnS, AIS/CdS QDs at open circuit voltage under simulated sunlight illumination. Photocatalytic hydrogen evolution experimental conditions: reaction solution, Na_2SO_3 (0.6 mol L $^{-1}$) aqueous solution (50 mL); catalyst loading, 3 mg; light source, 300 W Xe lamp with a cut off filter ($\lambda > 420$ nm) with the light intensity maintained at 600 mW cm $^{-2}$; reaction cell, Pyrex.

exhibiting the optimum activity for photocatalytic hydrogen generation in all samples.

To further support these conclusions, we calculated the wave functions of 1 S electrons and 1 S holes in the core/shell QDs to obtain a better understanding of their behavior and describe the enhanced hydrogen generation efficiency with the shell thickness increasing. The computed spatial probability distribution of $\psi_{\text{electron}}(r)$ and $\psi_{\text{hole}}(r)$ as a function of the QDs radius are shown in Fig. 4b and c. Both in AIS/ZnS and AIS/CdS QDs, the delocalization effect of 1 S electrons steadily intensify with the increase of shell thickness. For type-I band structure, this means that more electrons in the AIS core are likely to exceed the energy barrier and delocalized into the ZnS shell region in the AIS/ZnS QDs, but the hole remains restricted to the AIS core; these behaviors lead to a progressive reduction in the electron-hole spatial overlap and more photogenerated electrons are able to participate in the catalytic reaction. The hole wave function of AIS/CdS QDs exhibits leakage from the AIS core region with increasing CdS shell thickness, suggesting that more holes have crossed the energy barrier. Consequently, it is anticipated that more electrons and holes in AIS/CdS QDs will delocalize to the surface of the core, speeding up the transport of photogenerated electrons and holes to the reactants to achieve high efficiency solar energy conversion applications.

Time-resolved PL spectroscopy (TRPL) was used to investigate the relation between exciton recombination kinetics and the isolation

passivation of the shell and ligand. The PL decay of all QD samples can be well fit by three exponential decay function, showing time constants in Table S1. Fig. S10 displays time-resolved PL decay of AIS-OLA, AIS/ZnS-OLA and AIS/CdS-OLA QDs, with fitted average lifetimes of 245, 335 and 284 ns, respectively. Obviously, compared with AIS core, there is a prolonged lifetime for core/shell QDs, indicating that surface trap is effectively reduced, and the single exciton radiative recombination time between donor and acceptor is lengthened. The average lifetime of AIS/CdS-OLA QDs is lower than that of AIS/ZnS-OLA QDs, which is mainly attributed to the delocalization of electrons and holes in the CdS shell region, corresponding to the theoretical calculation and leading to an increased electron-hole wave function overlap. Furthermore, we investigated the TRPL of QDs after ligand exchange, as shown in Fig. 5a. The fitted average lifetimes of AIS/ZnS-S and AIS/CdS-S QDs are both much shorter and the weight of the fast decay components (τ_1) significantly increases following ligand exchange. This suggests that the S^{2-} could be considered as a surface trap as nonradiative recombination centers, leading to the decrease of PL intensity as shown in Fig. 2c. It was worth recalling that surface S^{2-} ligand can capture photogenerated holes and promote charge separation in our previous research [34,52]. Therefore, the S^{2-} ligands also decrease the barrier for hole transfer from the core/shell QDs to reactants in AIS/ZnS-S or AIS/CdS-S QDs, allowing the faster oxidation reaction.

To further investigate at the relaxation dynamics of photoexcited

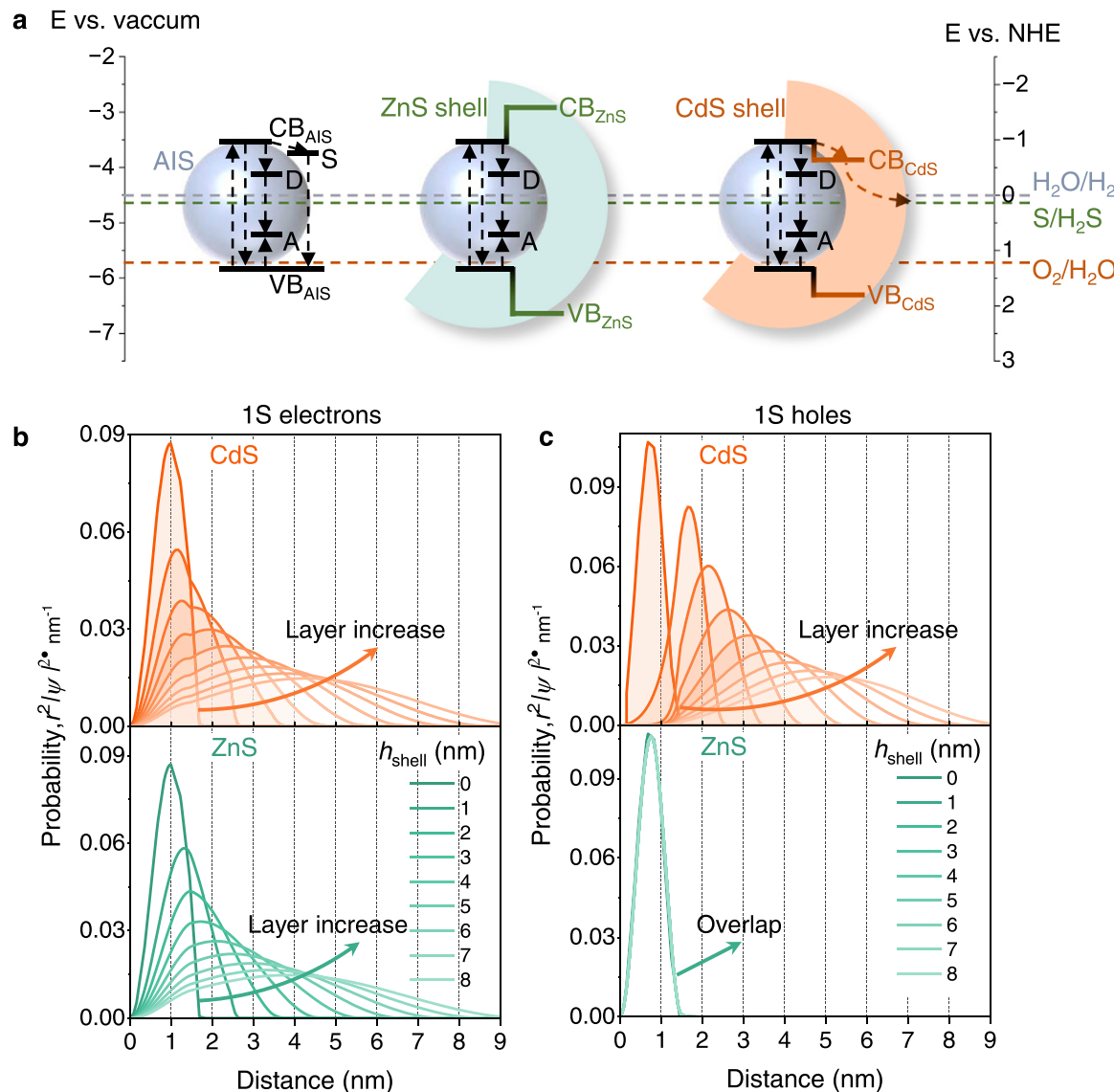


Fig. 4. Wave function calculations. a) Schematic diagram of the photoinduced process. The electron is trapped in either a sub-bandgap state (S) or a donor state (D), while the hole is trapped in an acceptor state (A); the arrows are a diagram of the charge carriers transfer process; the energy levels of AIS are based on our calculations, and those of ZnS shell are based on data from our literature [53]. The dotted line of $\text{H}_2\text{O}/\text{H}_2$ (gray) indicates the reduction potential of H_2 evolution, and the dotted line of $\text{S}/\text{H}_2\text{S}$ (green) and $\text{O}_2/\text{H}_2\text{O}$ (orange) represent the oxidation potential of H_2S and H_2O , respectively. Normalized radial distribution functions for AIS/ZnS and AIS/CdS core/shell QDs of b) the 1 S electron and c) 1 S hole.

carriers, we carried out transient absorption (TA) spectroscopy experiments with S^{2-} ligand-capped AIS and AIS/CdS QDs excited at 400 nm, corresponding pseudocolor TA spectra shown in Fig. S11 and S12. As shown in Fig. 5b, the pump-probe technique is frequently used in TA studies to monitor the transmission of a sample that has been excited by a fs laser pulse using a time-delayed probe pulse [54]. Fig. 5c and d show the TA spectra at early time delay, then Fig. 5e and f show the TA spectra at longer time delay for AIS-S and AIS/CdS-S QDs. TA spectra of AIS-S show two broad exciton bleach (XB) features at ~ 510 nm and 543 nm, labeled as B1 and B2, which can be attributed to excitonic absorption and sub-bandgap states (S-states) bleach, respectively. It is assumed that the generation of the B2 bleach feature in the AIS QD is related to the S-states of Ag based on the formation of a distinct bleach feature in CuInS_2 QD spectra [55]. After shell growth, it is observed that the AIS/CdS-S bleach feature narrows down. Furthermore, the absence of the B2 bleaching features of TA spectra of AIS/CdS-S QDs reveals that surface defects, such as vacancies and dangling bonds, were effectively passivated. For both AIS-S and AIS/CdS-S QDs, there is a low intensity

photoinduced absorption (PA) feature (Fig. 5c-f). Similar wide and featureless PA signal in TA spectra at longer time has also been observed in many QDs, including AgInS_2 , CdS and CdSe, which is the signature of electrons, holes or both, such as biexciton.

The dynamics of excited charge carriers has not clearly revealed by identifying these bleach signals. Thus, it is necessary to further fit and extract the information of transient bleach kinetics process based on the characteristic region (Fig. S13). Table S2 provides a summary of the corresponding exponential fitted parameters. The bleaching recovery kinetics shows the carrier depopulation dynamics from the CB edge, whereas the growing kinetics of the excitonic bleach position includes the electron cooling dynamics of various electronic states above the CB edge of QDs. At 510 nm (B1) for AIS and AIS/CdS, the bleach dynamics may be fitted with < 190 fs growth component ($\tau_{1\text{growth}}$), which denotes the electron cooling from the highly excited state to CB edge. The effective time constants of the bleaching recovery kinetics can be obtained, and the results indicate that the B1 recovery rates (τ_1 and τ_2) of AIS/CdS-S are faster than that of AIS-S. Compared with binary QDs,

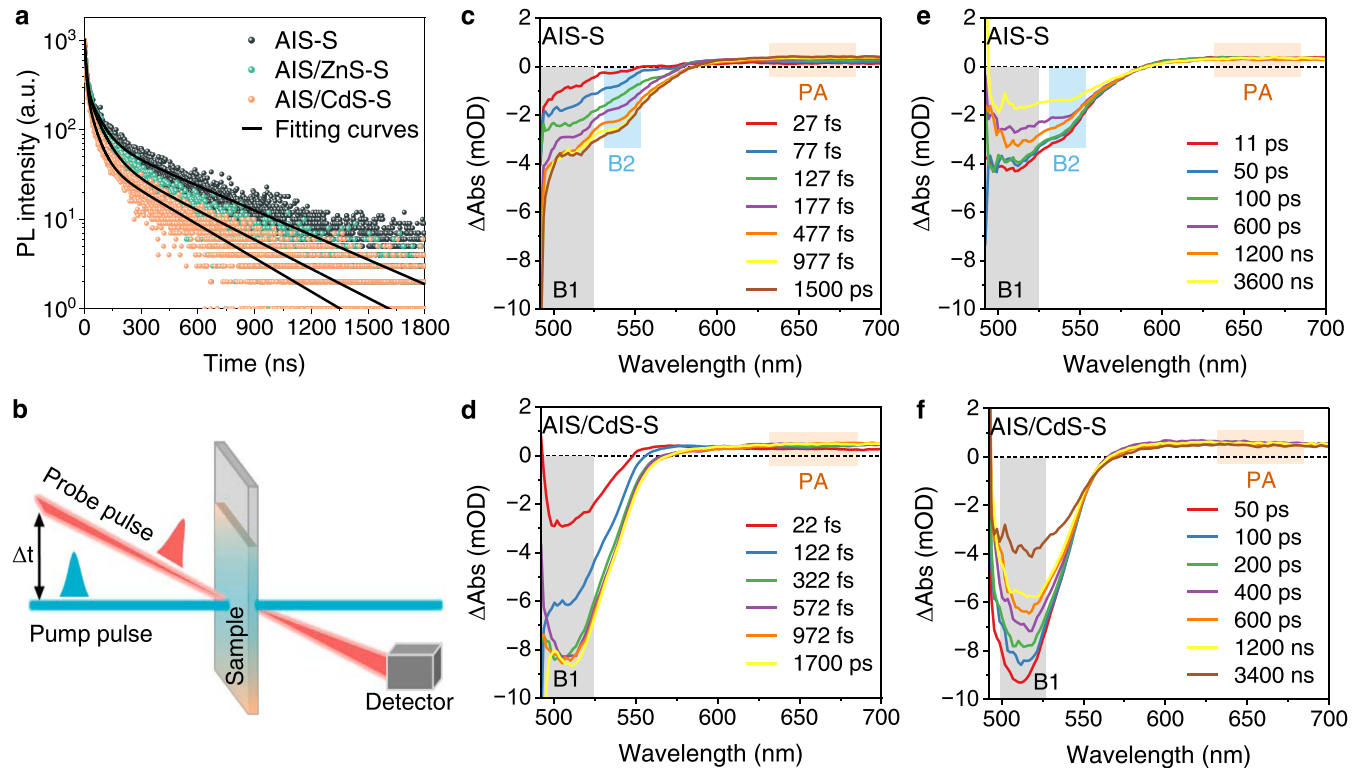


Fig. 5. TRPL spectra and TA spectra of QDs. a) TRPL of QDs-S, b) example transient absorption measurement. TA spectra at early time scale of c) AIS-S and d) AIS/CdS-S QDs. TA spectra at longer time scale of e) AIS-S and f) AIS/CdS-S QDs.

ternary QDs are more likely to form intrinsic defect sites, leading to a large Stokes shift, since they contain two cations with different radii [44, 56]. Meanwhile, due to the high specific surface area of nanomaterials, various QDs have many surface defects, such as vacancies and dangling bonds, being carrier recombination centers. Therefore, the intrinsic defect state recombination, surface defect state recombination and band-edge recombination are the main components of the ternary QDs radiation mechanism [57]. Radiation recombination center (D-A) is caused by intrinsic defects dominates, while band-edge recombination contributes the least to PL strength of ternary QDs [42]. Therefore, the quick recovery kinetics can be related to the transfer of electrons from the CB edge to the intrinsic defect [41, 55]. As a result, the quick recovery time constant ($\tau_1=200.7$ ps) can be attributed to the quick

transfer of electrons from the shallow level defect to the intrinsic defect for AIS-S QDs.

Nevertheless, the fast recovery component of AIS/CdS-S QDs cannot be straightforwardly identified as electronic transfer similar to AIS-S QDs due to the disappearance of B2 bleaching signal. As shown in Fig. 6a, compared with core-only QDs, the decreasing speed of absorbance (between B1 and B2 bleaching signals) is obviously more than that of AIS; the PL peak of AIS/CdS slightly blues-shifted, corresponded to the increase of band-edge recombination; and the disappearance of bleaching signal means that there may be different electron transfer channels. Due to passivation effect and the staggered band alignment of CdS shell to AIS, the fast recovery time constant ($\tau_1=164.9$ ps) of AIS/CdS-S QDs can be ascribed to electrons transferring from CdS CB

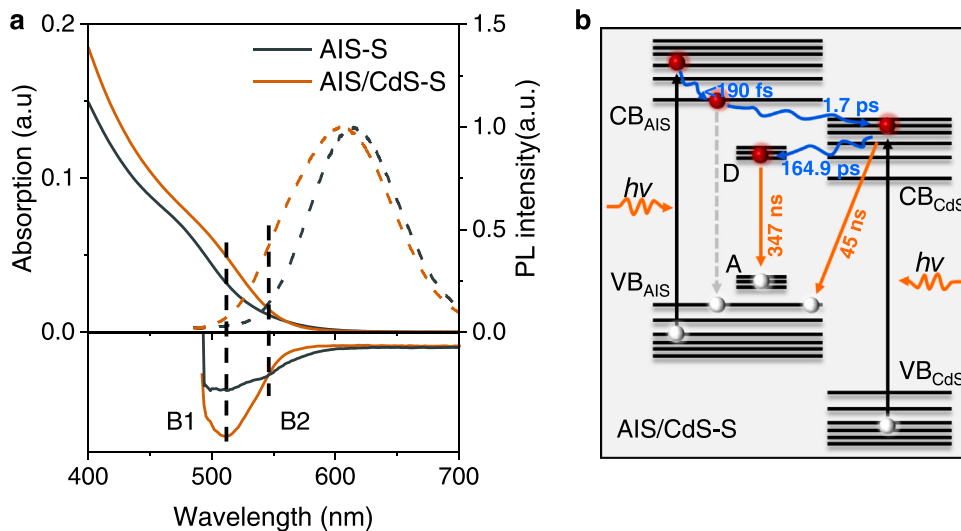


Fig. 6. a) The steady-state absorption (solid) and emission (dotted) spectra of AIS-S (black) and AIS/CdS-S (brown) QDs, including the TA spectrum of AIS-S and AIS/CdS at 50 ps. AIS/CdS-S (brown) contains B1 bleach band, while AIS (black) contains B1 and B2 bleach band. b) The illustration of carrier relaxation process in AIS/CdS-S QDs. Electrons transition from a more highly excited state to the conduction band edge, and then from the band edge to the conduction band of CdS and finally to the antisite state. Recombination primarily occurs via donor-acceptor pair of AIS and valence-band levels of CdS shell to AIS valence band levels.

levels to intrinsic defects. If only the kinetic trajectory at the B1 bleaching characteristic is observed, the entire charge carrier transfer kinetics cannot be obtained. In order to gain a deeper understanding of the charge carrier transfer dynamics of QDs, the transient bleaching dynamics of QDs at above (500 nm) band-edge, below band-edge are further compared here (Fig. S14 and S15), and the exponential fitting results are also summarized in Table S2. A growth component (<190 fs) and a fast recovery ($\tau_1 = 220.1$ ps for AIS-S and $\tau_1 = 60.9$ ps for AIS/CdS-S) can be obtained by fitting the bleach kinetics at 500 nm. The former is related to the rapid cooling of the electron to the band-edge state, while the latter indicates that the band-edge state of electron continues to transfer to a lower level. Furthermore, two times constants ($\tau_{1\text{growth}} < 190$ fs and $\tau_{2\text{growth}} = 1.9$ ps) are obtained by fitting the growth bleaching kinetics for AIS-S QDs below the band-edge (B2, 543 nm), and the subsequent recovery kinetics process can be fitted by bi-exponential. Here, $\tau_{1\text{growth}}$ can be attributed to electrons cooling to the conduction band edge, and $\tau_{2\text{growth}}$ represent the band edge transfer to the S-state of Ag associated sub-bandgap state. For AIS/CdS-S QDs, the bleach kinetics below the band edge (543 nm) can be fitted by bi-exponential growth $\tau_{1\text{growth}} < 190$ fs and $\tau_{2\text{growth}} = 1.7$ ps, which can be attributed to the similar electronic cooling, while the band-edge electron will transfer to the CB of CdS rather than S-state of Ag. What's more, combined with previous TRPL multi-exponential fitting results, we can obtain the carrier recombination lifetime of the S-states (or CdS CB levels) and intrinsic states. Finally, Fig. 6b and Fig. S16 depict a schematic diagram of the electron transition process in these QDs based on the aforementioned spectrum investigations, suggesting that the faster charge transfer of AIS/CdS-S than AIS QDs is the chief cause for its enhanced photocatalytic activity.

4. Conclusions

In summary, we have successfully designed and synthesized Type-II core/shell QDs with short-chain ligand to achieve photocatalytic H₂ evolution via H₂S splitting as hydrogen sources. The special synergistic effect of shell and S²⁻ ligand with dual charge-accepting-engineering effectively promotes the extraction of photo-generation carriers from QDs for efficient photocatalytic applications. The photocatalytic hydrogen evolution rate of the AIS/CdS-S is 4.16 times higher than that of the pristine AIS core, demonstrating a notable enhancement. More importantly, we have investigated carrier transfer and recombination dynamics in AIS core and AIS/CdS core/shell QDs following ligand exchange by wave function calculation and TA spectra, involving multiple states such as higher excited state, S-states and donor-acceptor states. The excited electrons are rapidly injected into the CdS shell from the AIS core within 1.7 ps, instead of moving to sub-bandgap states under pump light. It is reasonable to the increase in the rate of hydrogen evolution given the quick hole extraction from the AIS core and the fast band edge electron transfer. It is expected to this work will inspire more sparkling ideas for the practical application of the highly efficient photocatalytic over quantum dots catalysts and beyond toward resource utilization of pollutants and concurrent green H₂ generation.

CRediT authorship contribution statement

Anqiang Jiang: Conceptualization, Methodology, Investigation, Writing – original draft. **Fengying Zhang:** Formal analysis, Software, Methodology. **Tingyu Shuai:** Validation, Investigation. **Yubin Ke:** Methodology, Resources. **Peng Yang:** Investigation, Methodology. **Shan Yu:** Formal analysis, Methodology, Validation. **Heng Guo:** Conceptualization, Supervision., Funding acquisition. **Ying Zhou:** Supervision, Conceptualization, Project administration, Funding acquisition.

Declaration of Competing Interest

The authors declare that they have no known competing financial interests or personal relationships that could have appeared to influence the work reported in this paper.

Data availability

Data will be made available on request.

Acknowledgments

This work is financially supported by the National Natural Science Foundation of China (Grant No. 22109132, 22002123, 22178291), the Provincial Key Research and Development Project of Sichuan (2021YFSY0046, 2022YFSY0052, 2022NSFSC0023), International Science and Technology Cooperation Project of Chengdu (2021-GH02-00052-HZ). We acknowledge the China Spallation Neutron Source for the provision of instruments and time for SANS test. We thank Xiaoyan Zhang (Southwest Petroleum University) for the assistance with the XRD and XPS measurements.

Appendix A. Supporting information

Supplementary data associated with this article can be found in the online version at doi:[10.1016/j.apcatb.2023.122747](https://doi.org/10.1016/j.apcatb.2023.122747).

References

- [1] M. Van der Spek, C. Banet, C. Bauer, P. Gabrielli, W. Goldthorpe, M. Mazzotti, S. T. Munkejord, N.A. Røkke, N. Shah, N. Sunny, D. Sutter, J.M. Trusler, M. Gazzani, Perspective on the hydrogen economy as a pathway to reach net-zero CO₂ emissions in Europe, *Energy Environ. Sci.* 15 (2022) 1034–1077, <https://doi.org/10.1039/D1EE02118D>.
- [2] J. Rissman, C. Bataille, E. Masanet, N. Aden, W.R. Morrow, N. Zhou, N. Elliott, R. Dell, N. Heeren, B. Hückestein, J. Cresko, S.A. Miller, J. Roy, P. Fennell, B. Creminns, T. Koch Blank, D. Hone, E.D. Williams, S. de la Rue du Can, B. Sisson, M. Williams, J. Katzenberger, D. Burtraw, G. Sethi, H. Ping, D. Danielson, H. Lu, T. Lorber, J. Dinkel, J. Helseth, Technologies and policies to decarbonize global industry: review and assessment of mitigation drivers through 2070, *Appl. Energy* 266 (2020), 114848, <https://doi.org/10.1016/j.apenergy.2020.114848>.
- [3] D.W. Wakerley, M.F. Kuehn, K.L. Orchard, K.H. Ly, T.E. Rosser, E. Reisner, Solar-driven reforming of lignocellulose to H₂ with a CdS/CdO_x photocatalyst, *Nat. Energy* 2 (2017) 17021, <https://doi.org/10.1038/nenergy.2017.21>.
- [4] N.S. Lewis, Toward cost-effective solar energy use, *Science* 315 (2007) 798–801, <https://doi.org/10.1126/science.1137014>.
- [5] X.B. Li, C.H. Tung, L.Z. Wu, Semiconducting quantum dots for artificial photosynthesis, *Nat. Rev. Chem.* 2 (2018) 160–173, <https://doi.org/10.1038/s41570-018-0024-8>.
- [6] T. Hisatomi, K. Domen, Reaction systems for solar hydrogen production via water splitting with particulate semiconductor photocatalysts, *Nat. Catal.* 2 (2019) 387–399, <https://doi.org/10.1038/s41929-019-0242-6>.
- [7] B.A. Pinaud, J.D. Benck, L.C. Seitz, A.J. Forman, Z. Chen, T.G. Deutsch, B.D. James, K.N. Baum, G.N. Baum, S. Ardo, H. Wang, E. Miller, T.F. Jarillo, Technical and economic feasibility of centralized facilities for solar hydrogen production via photocatalysis and photoelectrochemistry, *Energy Environ. Sci.* 6 (2013) 1983–2002, <https://doi.org/10.1039/c3ee40831k>.
- [8] K. Takanabe, Photocatalytic water splitting: quantitative approaches toward photocatalyst by design, *ACS Catal.* 7 (2017) 8006–8022, <https://doi.org/10.1021/acscatal.7b02662>.
- [9] Y. Fang, Y. Hou, X. Fu, X. Wang, Semiconducting polymers for oxygen evolution reaction under light illumination, *Chem. Rev.* 122 (2022) 4204–4256, <https://doi.org/10.1021/acs.chemrev.1c00686>.
- [10] G. Zhang, X. Wang, Oxsulfide semiconductors for photocatalytic overall water splitting with visible light, *Angew. Chem. Int. Ed.* 58 (2019) 15580–15582, <https://doi.org/10.1002/anie.201909669>.
- [11] Q. Wang, K. Domen, Particulate photocatalysts for light-driven water splitting: mechanisms challenges and design strategies, *Chem. Rev.* 120 (2019) 919–985 (<https://doi.org/>).
- [12] B. Xia, Y. Zhang, B. Shi, J. Ran, K. Davey, S.Z. Qiao, Photocatalysts for hydrogen evolution coupled with production of value-added chemicals, *Small Methods* 4 (2020), 2000063, <https://doi.org/10.1002/smtb.202000063>.
- [13] Y. Zhao, C. Ding, J. Zhu, W. Qin, X. Tao, F. Fan, R. Li, C. Li, A hydrogen farm strategy for scalable solar hydrogen production with particulate photocatalysts, *Angew. Chem. Int. Ed.* 59 (2020) 9653–9658, <https://doi.org/10.1002/anie.202001438>.

[14] F. Costantino, P.V. Kamat, Do sacrificial donors donate H₂ in photocatalysis? *ACS Energy Lett.* 7 (2021) 242–246, <https://doi.org/10.1021/acsenergylett.1c02487>.

[15] Y.Z. Shangguan, Y.H. Zhou, R.J. Zheng, X.Z. Feng, Q.Y. Ge, R.H. Wang, D.Z. Yang, W.F. Wei, X.Y. Wu, J. Lin, H. Cheng, Bandgap engineering of tetragonal phase CuFeS₂ quantum dots via mixed-valence single-atomic Ag decoration for synergistic Cr(VI) reduction and RhB degradation, *Chin. Chem. Lett.* 32 (2021) 3450–3456, <https://doi.org/10.1016/j.cclet.2021.05.040>.

[16] M. Dan, Q. Zhang, S. Yu, A. Prakash, Y. Lin, Y. Zhou, Noble-metal-free MnS/In₂S₃ composite as highly efficient visible light driven photocatalyst for H₂ production from H₂S, *Appl. Catal. B* 217 (2017) 530–539, <https://doi.org/10.1016/j.apcatb.2017.06.019>.

[17] X. Zong, J.F. Han, B. Seger, H.J. Chen, G.Q. Lu, C. Li, L.Z. Wang, An integrated photoelectrochemical-chemical loop for solar-driven overall splitting of hydrogen sulfide, *Angew. Chem. Int. Ed.* 53 (2014) 4399–4403, <https://doi.org/10.1002/ange.201400571>.

[18] S. Yu, F. Wu, P. Zou, X.B. Fan, C. Duan, M. Dan, Z. Xie, Q. Zhang, F. Zhang, H. Zheng, Y. Zhou, Highly value-added utilization of H₂S in Na₂SO₃ solution over Ca-CdS nanocrystal photocatalysts, *Chem. Commun.* 56 (2020) 14227–14230, <https://doi.org/10.1039/d0cc05894g>.

[19] M. Dan, J. Xiang, J. Yang, F. Wu, C. Han, Y. Zhong, K. Zheng, S. Yu, Y. Zhou, Beyond hydrogen production: solar-driven H₂S-donating value-added chemical production over Mn_xCd_{1-x}S/CdyMn_{1-y}S catalyst, *Appl. Catal. B* 284 (2021), 119706, <https://doi.org/10.1016/j.apcatb.2020.119706>.

[20] M. Dan, F. Wu, J. Xiang, Y. Cao, Y. Zhong, K. Zheng, Y. Liu, Z.-Q. Liu, S. Yu, Y. Zhou, A dual-interfacial system with well-defined spatially separated redox-sites for boosting photocatalytic overall H₂S splitting, *Chem. Eng. J.* 423 (2021), 130201, <https://doi.org/10.1016/j.cej.2021.130201>.

[21] M. Dan, S. Wei, D.E. Doronkin, Y. Li, Z. Zhao, S. Yu, J.D. Grunwaldt, Y. Lin, Y. Zhou, Novel MnS/(In_xCu_{1-x})₂S₃ composite for robust solar hydrogen sulphide splitting via the synergy of solid solution and heterojunction, *Appl. Catal. B* 243 (2019) 790–800, <https://doi.org/10.1016/j.apcatb.2018.11.016>.

[22] K. Li, B. Chai, T. Peng, J. Mao, L. Zan, Preparation of AgIn₅S₈/TiO₂ heterojunction nanocomposite and its enhanced photocatalytic H₂ production property under visible light, *ACS Catal.* 3 (2013) 170–177, <https://doi.org/10.1021/cs300724r>.

[23] Q. Zhang, M. Wang, M. Ao, Y. Luo, A. Zhang, L. Zhao, L. Yan, F. Deng, X. Luo, Solvothermal synthesis of Z-scheme AgIn₅S₈/Bi₂WO₆ nano-heterojunction with excellent performance for photocatalytic degradation and Cr(VI) reduction, *J. Alloy. Compd.* 805 (2019) 41–49, <https://doi.org/10.1016/j.jallcom.2019.06.331>.

[24] H. Guo, B. Luo, J. Wang, B.-J. Wang, X. Huang, J. Yang, W.-X. Gong, Y. Zhou, X.-B. Niu, Boosting photoelectrochemical hydrogen generation on Cu-doped AgIn₅S₈/ZnS colloidal quantum dot sensitized photoanodes via shell-layer homojunction defect passivation, *J. Mater. Chem. A* 8 (2020) 24655–24663, <https://doi.org/10.1039/d0ta09474a>.

[25] C.Y. Ji, M. Lu, H. Wu, X.Y. Zhang, X.Y. Shen, X. Wang, Y. Zhang, Y.D. Wang, W.W. Yu, 1,2-Ethanediol treatment for AgIn₅S₈/ZnS quantum dot light-emitting diodes with high brightness, *ACS Appl. Mater. Interfaces* 9 (2017) 8187–8193, <https://doi.org/10.1021/acsami.6b16238>.

[26] H. Guo, J. Liu, B. Luo, X. Huang, J. Yang, H. Chen, L. Shi, X. Liu, D. Benetti, Y. Zhou, G.S. Selopal, F. Rosei, Z. Wang, X. Niu, Unlocking the effects of Cu doping in heavy-metal-free AgIn₅S₈ quantum dots for highly efficient photoelectrochemical solar energy conversion, *J. Mater. Chem. C* 9 (2021) 9610–9618, <https://doi.org/10.1039/dltc01624e>.

[27] Cdm Donega, Synthesis and properties of colloidal heteronanoocrystals, *Chem. Soc. Rev.* 40 (2011) 1512–1546, <https://doi.org/10.1039/c0cs00055h>.

[28] Y. Cao, Q. Zheng, Z. Rao, R. Zhang, Z. Xie, S. Yu, Y. Zhou, InP quantum dots on g-C₃N₄ nanosheets to promote molecular oxygen activation under visible light, *Chin. Chem. Lett.* 31 (2020) 2689–2692, <https://doi.org/10.1016/j.cclet.2020.07.032>.

[29] R. Ghosh Chaudhuri, S. Paria, Core/shell nanoparticles: classes properties synthesis mechanisms characterization and applications, *Chem. Rev.* 112 (2012) 2373–2433, <https://doi.org/10.1021/cr100449n>.

[30] Q. Zheng, Y.H. Cao, N.J. Huang, R.Y. Zhang, Y. Zhou, Selective exposure of BiOI oxygen-rich {110} facet induced by BN nanosheets for enhanced photocatalytic oxidation performance, *Acta Phys. Chim. Sin.* 37 (2021), 2009063, <https://doi.org/10.3866/PKU.WHXB202009063>.

[31] H. Li, H. Gong, Z. Jin, In₂O₃-modified three-dimensional nanoflower MoS_x form S-scheme heterojunction for efficient hydrogen production, *Acta Phys. Chim. Sin.* 38 (2022), 2201037, <https://doi.org/10.3866/PKU.WHXB202201037>.

[32] A. Nag, M.V. Kovalenko, J.S. Lee, W. Liu, B. Spokoyny, D.V. Talapin, Metal-free inorganic ligands for colloidal nanocrystals: S²⁻, HS⁻, Se²⁻, HSe⁻, Te²⁻, HTe⁻, TeS₃²⁻, OH⁻, and NH₂ as surface ligands, *J. Am. Chem. Soc.* 133 (2011) 10612–10620, <https://doi.org/10.1021/ja2029415>.

[33] K. Sun, Y. Zhao, J. Yin, J. Jin, H. Liu, P. Xi, Surface modification of NiCo₂O₄ nanowires using organic ligands for overall water splitting, *Acta Phys. Chim. Sin.* 38 (2021), 2107005, <https://doi.org/10.3866/PKU.WHXB202107005>.

[34] S. Yu, X.B. Fan, X. Wang, J. Li, Q. Zhang, A. Xia, S. Wei, L.Z. Wu, Y. Zhou, G. R. Patzke, Efficient photocatalytic hydrogen evolution with ligand engineered all-inorganic InP and InP/ZnS colloidal quantum dots, *Nat. Commun.* 9 (2018) 4009, <https://doi.org/10.1038/s41467-018-06294-y>.

[35] K.E. Knowles, H.D. Nelson, T.B. Kilburn, D.R. Gamelin, Singlet-triplet splittings in the luminescent excited states of colloidal Cu⁺:CdSe, Cu⁺:InP, and CuInS₂ nanocrystals: charge-transfer configurations and self-trapped excitons, *J. Am. Chem. Soc.* 137 (2015) 13138–13147, <https://doi.org/10.1021/jacs.5b08547>.

[36] M. Jones, G.D. Scholes, On the use of time-resolved photoluminescence as a probe of nanocrystal photoexcitation dynamics, *J. Mater. Chem.* 20 (2010) 3533–3538, <https://doi.org/10.1039/c000165a>.

[37] A.C. Berends, M.J.J. Mangnus, C. Xia, F.T. Rabouw, C. de Mello Donega, Optoelectronic properties of ternary I-III-VI₂ semiconductor nanocrystals: bright prospects with elusive origins, *J. Phys. Chem. Lett.* 10 (2019) 1600–1616, <https://doi.org/10.1021/acs.jpclett.8b03653>.

[38] S. Jeong, H.G. Yoon, N.S. Han, J.H. Oh, S.M. Park, B.K. Min, Y.R. Do, J.K. Song, Band-gap states of AgIn₅S₈ and ZnS-AgIn₅S₈ nanoparticles, *J. Phys. Chem. C* 121 (2017) 3149–3155, <https://doi.org/10.1021/acs.jpcc.7b00043>.

[39] S.M. Kobsos, P.V. Kamat, Indium-rich AgIn₅S₈ quantum dots-Ag⁺/Zn²⁺ dependent photophysics and photovoltaics, *J. Phys. Chem. C* 122 (2018) 14336–14344, <https://doi.org/10.1021/acs.jpcc.8b03001>.

[40] D.H. Jara, K.G. Samplecoskie, P.V. Kamat, Two distinct transitions in Cu_xInS₂ quantum dots: bandgap versus sub-bandgap excitations in copper-deficient structures, *J. Phys. Chem. Lett.* 7 (2016) 1452–1459, <https://doi.org/10.1021/acs.jpclett.6b000571>.

[41] T. Debnath, H.N. Ghosh, Ternary metal chalcogenides: into the exciton and biexciton dynamics, *J. Phys. Chem. Lett.* 10 (2019) 6227–6238, <https://doi.org/10.1021/acs.jpclett.9b01596>.

[42] B. Mao, C.-H. Chuang, J. Wang, C. Burda, Synthesis and photophysical properties of ternary I-III-VI₂ AgIn₅S₈ nanocrystals: intrinsic versus surface states, *J. Phys. Chem. C* 115 (2011) 8945–8954, <https://doi.org/10.1021/jp2011183>.

[43] D.E. Nam, W.-S. Song, H. Yang, Facile air-insensitive solvothermal synthesis of emission-tunable CuInS₂/ZnS quantum dots with high quantum yields, *J. Mater. Chem.* 21 (2011) 18220–18226, <https://doi.org/10.1039/c1jm12437d>.

[44] L. Li, A. Pandey, D.J. Werder, B.P. Khanal, J.M. Pietryga, V.I. Klimov, Efficient synthesis of highly luminescent copper indium sulfide-based core/shell nanocrystals with surprisingly long-lived emission, *J. Am. Chem. Soc.* 133 (2011) 1176–1179, <https://doi.org/10.1021/ja108261h>.

[45] S.P. Hong, H.K. Park, J.H. Oh, H. Yang, Y.R. Do, Comparisons of the structural and optical properties of o-AgIn₅S₈, t-AgIn₅S₈, and c-AgIn₅S₈ nanocrystals and their solid-solution nanocrystals with ZnS, *J. Mater. Chem.* 22 (2012) 18939, <https://doi.org/10.1039/c2jm33879c>.

[46] T. Li, A.J. Senesi, B. Lee, Small angle X-ray scattering for nanoparticle research, *Chem. Rev.* 116 (2016) 11128–11180, <https://doi.org/10.1021/acs.chemrev.5b00690>.

[47] H.H. Wei, C.M. Evans, B.D. Swartz, A.J. Neukirch, J. Young, O.V. Prezhdo, T. D. Krauss, Colloidal semiconductor quantum dots with tunable surface composition, *Nano Lett.* 12 (2012) 4465–4471, <https://doi.org/10.1021/nl3012962>.

[48] S.A. Ivanov, A. Piryatinski, J. Nanda, S. Tretiak, K.R. Zavadil, W.O. Wallace, D. Werder, V.I. Klimov, Type-II Core/Shell CdS/ZnSe nanocrystals: synthesis, electronic structures and spectroscopic properties, *J. Am. Chem. Soc.* 129 (2007) 11708–11719, <https://doi.org/10.1021/ja068351m>.

[49] J.P. Philbin, E. Rabani, Auger recombination lifetime scaling for type I and quasi-type II core/shell quantum dots, *J. Phys. Chem. Lett.* 11 (2020) 5132–5138, <https://doi.org/10.1021/acs.jpclett.0c01460>.

[50] L. Chensha, W. Jiawen, H. Ju, W. Binsong, Q. Yang, H. Zhengjia, Fabrication of N-CQDs@W₁₈O₄₉ heterojunction with enhanced charge separation and photocatalytic performance under full-spectrum light irradiation, *Chin. Chem. Lett.* 32 (2021) 3180–3184, <https://doi.org/10.1016/j.cclet.2021.03.018>.

[51] C.H. Chuang, T.L. Doane, S.S. Lo, G.D. Scholes, C. Burda, Measuring electron and hole transfer in core/shell nanoheterostructures, *ACS Nano* 5 (2011) 6016–6024, <https://doi.org/10.1021/nn201788f>.

[52] Y. Liu, Y. Zhou, M. Abdellah, W. Lin, J. Meng, Q. Zhao, S. Yu, Z. Xie, Q. Pan, F. Zhang, T. Pullerits, K. Zheng, Inorganic ligands-mediated hole attraction and surface structural reorganization in InP/ZnS QD photocatalysts studied via ultrafast visible and midinfrared spectroscopies, *Sci. China Mater.* 65 (2022) 2529–2539, <https://doi.org/10.1007/s40843-021-1992-3>.

[53] K. Boldt, C. Ramanan, A. Chanaewa, M. Werheid, A. Eychmüller, Controlling charge carrier overlap in type-II ZnSe/ZnS/CdS core-barrier-shell quantum dots, *J. Phys. Chem. Lett.* 6 (2015) 2590–2597, <https://doi.org/10.1021/acs.jpclett.5b01144>.

[54] V.I. Klimov, D.W. McBranch, Femtosecond high-sensitivity chirp-free transient absorption spectroscopy using kilohertz lasers, *Opt. Lett.* 23 (1998) 277–279, <https://doi.org/10.1364/ol.23.000277>.

[55] J. Dana, T. Debnath, H.N. Ghosh, Involvement of sub-bandgap states in subpicosecond exciton and biexciton dynamics of ternary AgIn₅S₈ nanocrystals, *J. Phys. Chem. Lett.* 7 (2016) 3206–3214, <https://doi.org/10.1021/acs.jpclett.6b01341>.

[56] O. Yarema, M. Yarema, D. Bozyigit, W.M.M. Lin, V. Wood, Independent composition and size control for highly luminescent indium-rich silver indium selenide nanocrystals, *ACS Nano* 9 (2015) 11134–11142, <https://doi.org/10.1021/acsnano.5b04636>.

[57] C. Xia, P. Tamarat, L. Hou, S. Busatto, J.D. Meeldijk, C. de Mello Donega, B. Lounis, Unraveling the emission pathways in copper indium sulfide quantum dots, *ACS Nano* 15 (2021) 17573–17581, <https://doi.org/10.1021/acsnano.1c04909>.